Universität Karlsruhe (TH)
Institut für Baustatik

A Finite Element Formulation for the Simulation of Propagating Delaminations in Layered Composite Structures

W. Wagner, F. Gruttmann, W. Sprenger

Mitteilung 2(2000)

Universität Karlsruhe (TH)
Institut für Baustatik

A Finite Element Formulation for the Simulation of Propagating Delaminations in Layered Composite Structures

W. Wagner, F. Gruttmann, W. Sprenger

Mitteilung 2(2000)

Prof. Dr.–Ing. W. Wagner
Institut für Baustatik
Universität Karlsruhe
Postfach 6980
76128 Karlsruhe

Telefon: (0721) 608–2280
Telefax: (0721) 608–6015
E–mail: bs@.uni-karlsruhe.de
Internet: http://www.bs.uni-karlsruhe.de

A Finite Element Formulation for the Simulation of Propagating Delaminations in Layered Composite Structures

W. Wagner*, F. Gruttmann+, W. Sprenger*

* Institut für Baustatik, Universität Karlsruhe (TH), Kaiserstr. 12, D-76131 Karlsruhe, Germany

+ Institut für Statik, Technische Universität Darmstadt, Alexanderstr. 7, D-64283 Darmstadt, Germany

Abstract

This paper presents a finite element method to simulate growing delaminations in composite structures. The delamination process, using an inelastic material law with softening, takes place within an interface layer having a small, but non–vanishing thickness. A stress criterion is used to detect the critical points. To prevent mesh dependent solutions a regularization technique is applied. The artificial viscosity leads to corresponding stiffness matrices which guarantee stable equilibrium iterations. The essential material parameter which describes the delamination process is the critical energy release rate. The finite element calculations document the robustness and effectivity of the developed model. Extensive parameter studies are performed to show the influence of the introduced geometrical and material quantities.

Keywords: Composite laminates, delamination, viscoplasticity, finite elements

1 Introduction

One of the most dangerous failure modes in composite laminates is delamination, see Fig. 1. The loss of strength and stiffness may reduce the lifetime in a significant way. To utilize the full potential of composites it is necessary to analyze initiation and growth of delamination which may be a basis of appropriate construction measures.

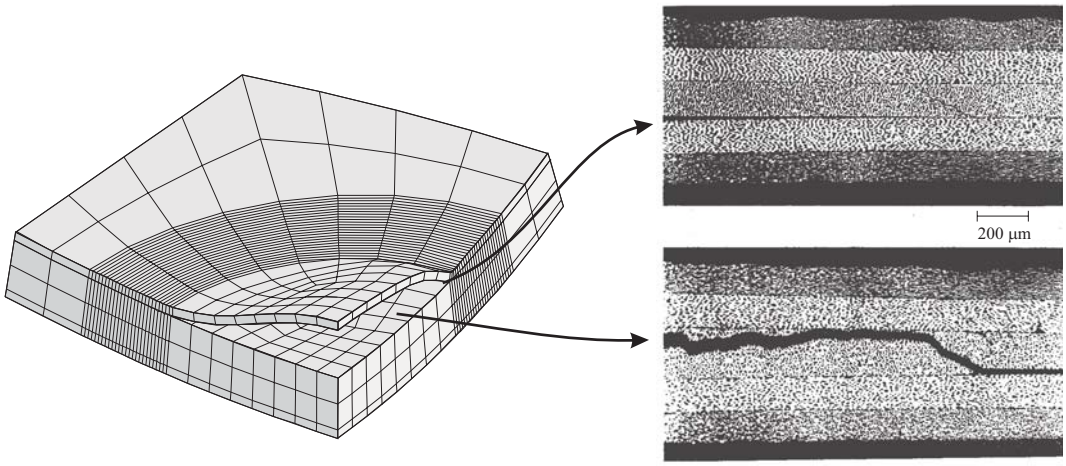

Figure 1: Delamination problem: finite element mesh and experiment

Due to the complexity of the underlying mathematical model, usually numerical procedures are applied to compute increasing delaminations. The so–called first–ply failure analysis yields the location where damage starts, see e.g. *Lee* [1]. Several authors use stress–based criteria to predict different failure modes, e.g. *Hashin* [2]. If the criterion is not fulfilled stiffness parameters are reduced or set to zero. The procedure may not work if the stress field is singular. Another disadvantage is a lack of robustness within the equilibrium iterations. This holds especially for geometrical nonlinear calculations. Numerical investigations show that mesh refinement not necessarily leads to a converged solution.

Other authors use a fracture mechanics approach. When the energy related to the newly opened crack-surface exceeds a critical value, the crack extends. In so-called virtual crack-extension or crack-closure methods the energy release rate is calculated using the nodal forces and displacements within the finite element method, *Davidson* [3], *Wang et al.* [4] and *Teßmer* [5]. A considerable number of iterations may be necessary until a configuration is found where equilibrium and delamination criterion are fulfilled.

In some papers interface elements with double nodes are used to map the geometric discontinuities arising within the delamination process. *Schellekens and de*

Borst [6] developed plane strain elements and associated interface elements with cubic interpolation functions. *Crisfield et al.* [7] modified the concept along with eight–node quadrilateral plane strain elements. In their approach the constitutive equations are formulated directly in terms of crack opening displacements. Interlaminar strains cannot be computed, since the thickness of the interface elements vanishes.

The goal of this paper is to present an effective finite element tool for the numerical analysis of delaminations in layered composites. The essential features and novel aspects are summarized as follows.

To obtain the complete three–dimensional stress state we discretize the laminated composite structures with eight–noded hexahedral elements, documented in *Klinkel et al.* [8]. Due to special interpolation techniques based on mixed variational principles the elements are able to predict the stress state even for very thin structures. In large scale problems the use of 3D elements may not be practical. To reduce the numerical effort coupled 2D/3D computations have been discussed in *Wagner and Gruttmann* [9]. For this purpose a special interface element has been developed, which allows the coupling of shell elements with hexahedral elements.

Delamination takes place in interface layers with small but not vanishing thickness. The interlaminar stresses are determined using an inelastic material law with softening. The slope of the softening curve is determined by the critical energy release rate, the thickness of the interface layer and the tensile strength of the laminate in thickness direction. Complete delamination occurs if the newly opened surface is free of stresses. To avoid mesh dependent solutions a regularization technique is applied.

The paper is arranged as follows: We start with the description of the interface element and the delamination model. Hence, the formulations of the rate independent plasticity model and the regularization concept are given. Four examples are investigated, where extensive parameter studies are performed to show the influence of the introduced geometrical and material quantities. For the so–called double cantilever beam good agreement with experimental results could be shown. Furthermore a plate strip and a plate with given delamination zone are investigated. Finally, propagating delaminations within a carbon–fibre reinforced composite plate are computed and compared with experimental results.

2 Delamination model

Delamination of layered composites usually occurs together with damage within the plys. However, the complicated interaction between the different failure modes is not considered in the present paper. To account for the three–dimensional stress state, which typically occurs in composite structures, the discretization is performed using hexahedral elements. The standard isoparametric eight–node element with trilinear shape functions is improved to reduce the well–known locking effects when discretizing thin structures. Applying an assumed strain method (ANS), the transverse shear strains are independently interpolated, see e.g. *Bathe and Dvorkin* [10]. Furthermore, the thickness strains are approximated according to the paper of *Betsch and Stein* [11]. The membrane behaviour is improved by applying the enhanced assumed strain method (EAS) with five parameters (*Simo and Rifai* [12]). The variational formulation and detailed finite element equations of the ANS–EAS5–element are given in *Klinkel et al.* [8].

2.1 Interface layer

Fig. 2 shows a finite element discretization of a plate strip using eight–node elements. The interface layers, with thickness h_t, are positioned in those regions where delamination is expected. Our numerical investigations showed that the behaviour of the global composite structure remains practically unaltered for thickness ratios of $h_t/h \leq 10^{-2}$, where h denotes the thickness of the total laminate, see Fig. 3. Using a material formulation, the variational equations

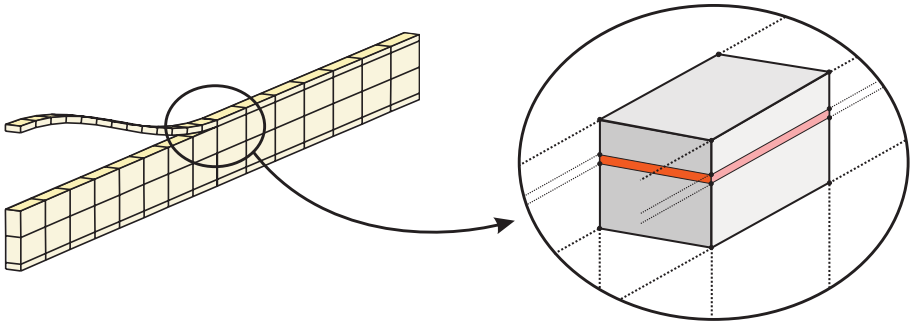

Figure 2: Plate strip with delaminated layer and interface element (dark shaded)

are written in terms of the Second Piola–Kirchhoff stress tensor $\mathbf{S}$ and the work conjugate Green–Lagrangian strain tensor $\mathbf{E}$. The tensor components refer to different basis systems, where the transformations are given in *Sprenger et al.* [13].

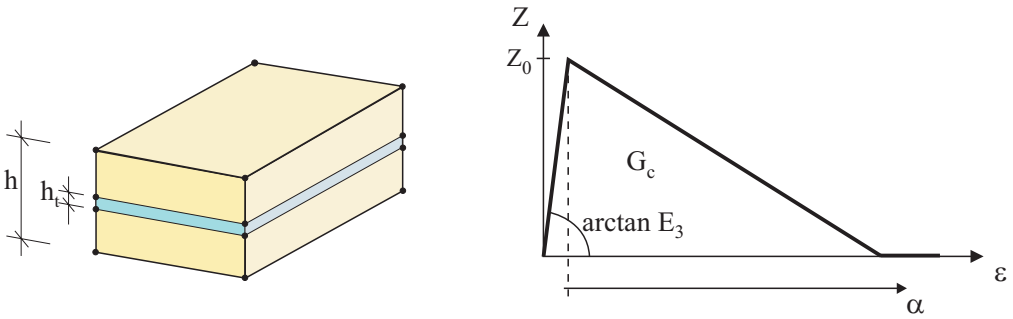

Figure 3: Interface layer and softening function

In this paper the criterion of *Hashin* [2] in terms of the interlaminar normal stresses S^{33} and shear stresses S^{13} and S^{23} is used to predict the location where delamination occurs

$$\frac{(S^{33})^2}{Z_0^2} + \frac{(S^{13})^2 + (S^{23})^2}{R_0^2} \leq 1\,. \tag{1}$$

Here, Z_0 and R_0 denote the tensile strength in thickness direction and the shear strength of the laminate, respectively. In (1) the stress components refer to a local Cartesian coordinate system, [13]. The criterion of Hashin can only be formulated in terms of Second Piola Kirchhoff stresses, if the application is restricted to small deformations. Otherwise the transformation to the Cauchy stress tensor $\boldsymbol{\sigma}$ has to be considered.

Furthermore, linear softening behaviour according to Fig. 3 is introduced

$$Z(\alpha) = Z_0\,(1 - \mu\alpha) \geq 0 \qquad \text{with} \quad \mu > 0\,, \tag{2}$$

where the internal variable α denotes the equivalent inelastic strain. The critical energy release G_c rate corresponds to the area under the softening curve multiplied with h_t, since in the present model the energy is dissipated within the interface layer of thickness h_t, thus

$$G_c = \frac{Z_0^2 h_t}{2}\,(\frac{1}{E_3} + \frac{1}{Z_0\mu})\,, \tag{3}$$

where E_3 denotes the elastic modulus in thickness direction. If the elastic deformations are negligible, which means that the first term in the sum cancels out, the softening parameter μ can easily be determined from (3) as

$$\mu \;=\; \frac{Z_0\; h_t}{2\; G_c}\,. \tag{4}$$

Delamination is defined, when the absolute value of the interlaminar stress vector vanishes. From (2) and $Z(\alpha) = 0$ follows $\alpha = \dfrac{2\; G_c}{Z_0\; h_t}$.

2.2 The rate–independent plasticity model

With the assumption of small strains the Green–Lagrange strain tensor $\mathbf{E}$ and the associated rate can be additively decomposed in an elastic and an inelastic part. The elastic part follows from the linear constitutive law, assuming transversally–isotropic material behaviour. The inelastic strain rates and the evolution law for the equivalent plastic strains are given with the inelastic multiplier $\dot{\lambda}$. Summarizing, the rate–independent plasticity model is written as

$$\begin{aligned} \dot{\mathbf{E}} &= \dot{\mathbf{E}}^{el} + \dot{\mathbf{E}}^{in} \,, \\ \dot{\mathbf{E}}^{el} &= \mathbf{C}^{-1}\, \dot{\mathbf{S}} \,, \\ \dot{\mathbf{E}}^{in} &= \dot{\mathbf{E}}^{pl} \;=\; \dot{\lambda}\, \mathbf{N} \,, \\ \dot{\alpha} &= \dot{\lambda} \,. \end{aligned} \tag{5}$$

The constitutive tensor $\mathbf{C}$ in terms of the elasticity constants E_i, G_{ij} and ν_{ij} is described in [13]. Here $\mathbf{N}$ denotes the gradient of the yield function $F(\mathbf{S}, \alpha)$. The fracture criterion (1) is reformulated and extended by the softening function (2) as follows

$$F(\mathbf{S}, \alpha) = g(\mathbf{S}) - Z(\alpha) \tag{6}$$

with

$$g(\mathbf{S}) = \sqrt{\mathbf{S} \cdot \mathbf{A}\mathbf{S}} \,, \qquad \mathbf{A} = \mathrm{Diag}\left[0,\; 0,\; 1,\; 0,\; \left(\frac{Z_0}{R_0}\right)^2,\; \left(\frac{Z_0}{R_0}\right)^2\right] . \tag{7}$$

The components of $\mathbf{A}$ are given here in matrix notation. For $\alpha = 0$ eq. (6) is another representation of (1), thus it is formulated with respect to a local Cartesian coordinate system.

The loading–unloading conditions must hold in (5) - (6)

$$\dot{\lambda} \geq 0 \;, \quad F \leq 0 \;, \quad \dot{\lambda} F = 0 \;\; . \tag{8}$$

In case of loading with $\dot{\lambda} > 0$ the rate equations (5) considering $\mathbf{N} = \mathbf{A}\,\mathbf{S}/g$ are approximately time–integrated using a backward Euler integration algorithm. Within a time step $t_{n+1} = t_n + \Delta t$ one obtains, after some algebraic manipulations, the stress tensor and the parameter α

$$\begin{aligned} \mathbf{S}_{n+1} &= \left[\mathbf{C}^{-1} + \tfrac{\lambda}{Z(\alpha_{n+1})}\, \mathbf{A}\right]^{-1} \left[\mathbf{E}_{n+1} - \mathbf{E}_n^{pl}\right] \;=\; \mathbf{P}\; \mathbf{E}^{tr} \,, \\ \alpha_{n+1} &= \alpha_n + \lambda \,. \end{aligned} \tag{9}$$

Here, the notation $\lambda := \Delta t \dot{\lambda}_{n+1}$, $\mathbf{S}_{n+1} = \mathbf{S}(t_{n+1})$ and $\alpha_{n+1} = \alpha(t_{n+1})$ is used.

The linearization of the stress tensor yields the consistent tangent operator

$$\bar{\mathbf{D}} = \mathbf{P} - \frac{\mathbf{P}\mathbf{N} \otimes \mathbf{P}\mathbf{N}}{\mathbf{N} \cdot \mathbf{P}\mathbf{N} + H} \qquad , \qquad H = \frac{Z'}{1 - \lambda \frac{Z'}{Z}} \,, \tag{10}$$

with $Z' := \mathrm{d}Z/\mathrm{d}\alpha$. If for $Z > 0$ the softening parameter μ increases certain values, negative diagonal terms in $\bar{\mathbf{D}}$ occur. In this case the global iteration process to solve the equilibrium equations becomes unstable. For $Z = 0$ the expressions for $\mathbf{P}$ and H are undefined. This can be avoided introducing a tolerance.

2.3 Viscoplastic regularization

To prevent the described numerical instabilities, we use a viscoplastic regularization technique. The strain rates are introduced according to the approach of Duvaut and Lions [14]

$$\begin{aligned} \dot{\mathbf{E}}^{in} &= \dot{\mathbf{E}}^{vp} = \frac{1}{\eta}\mathbf{C}^{-1}\left(\mathbf{S} - \bar{\mathbf{S}}\right) , \\ \dot{\alpha} &= -\frac{1}{\eta}\left(\alpha - \bar{\alpha}\right) , \end{aligned} \tag{11}$$

where η denotes the normalized viscosity parameter. In the present case η is a purely numerical parameter which has the meaning of a relaxation time. The automatic control for each integration point is presented in the next section. The stresses $\bar{\mathbf{S}}$ and equivalent plastic strains $\bar{\alpha}$ denote the solutions of the rate–independent theory.

Substitution of eq. $(5)_2$ and $(11)_1$ into eq. $(5)_1$ yields another representation of (11)

$$\begin{aligned} \dot{\mathbf{S}} + \frac{1}{\eta}\mathbf{S} &= \mathbf{C}\,\dot{\mathbf{E}} + \frac{1}{\eta}\bar{\mathbf{S}} , \\ \dot{\alpha} + \frac{1}{\eta}\alpha &= \frac{1}{\eta}\bar{\alpha} . \end{aligned} \tag{12}$$

The solutions of the homogeneous differential equations are obtained analytically. The inhomogeneous part is solved approximately using a backward Euler integration algorithm, see also [15]. Introducing $\mathbf{S}_n = \mathbf{S}(t_n)$, $\delta = \Delta t/\eta$ and $\beta = \exp(-\delta)$ we end up with

$$\begin{aligned} \mathbf{S}_{n+1} &= \beta\,\mathbf{S}_n + (1-\beta)\,\bar{\mathbf{S}}_{n+1} + \frac{1-\beta}{\delta}\,\mathbf{C}\,\Delta\mathbf{E} , \\ \alpha_{n+1} &= \beta\,\alpha_n + (1-\beta)\,\bar{\alpha}_{n+1} . \end{aligned} \tag{13}$$

The viscoplastic tangent matrix follows immediately with

$$\mathbf{D} = \frac{\mathrm{d}\mathbf{S}}{\mathrm{d}\mathbf{E}} = \frac{1-\beta}{\delta}\,\mathbf{C} + (1-\beta)\,\bar{\mathbf{D}} , \tag{14}$$

The first term in (14) leads to positive diagonal entries in the viscoplastic tangent matrix, where the factor δ implies that with decreasing η the time increment Δt

has to be reduced, to obtain the desired effect. The symmetric matrix $\mathbf{D}$ is necessary to setup the tangent stiffness matrix for the equilibrium iteration.

The calculation of the viscoplastic stresses and associated linearizations is summarized in the flowchart in Table 1. In a standard way the algorithm requires the storage of the inelastic quantities of time t_n.

- Trial elastic state, time step $t_{n+1} = t_n + \Delta t$

  $\mathbf{E}^{tr} = \mathbf{E}_{n+1} - \mathbf{E}_n^{vp}, \quad \mathbf{S} = \mathbf{C}\,\mathbf{E}^{tr}$

- Check fracture criterion, if $F(\mathbf{S}, \alpha_n) \leq 0 \quad \Rightarrow$ elastic state

- Start of local iteration: $l = 1$, $\mathbf{S}_l = \mathbf{S}$, $\alpha_l = \alpha_n$, $\lambda_l = 0$

  1. $Z_l = Z(\alpha_l)$, $Z_l' = \mathrm{d}Z(\alpha_l)/\mathrm{d}\alpha$
  2. $\mathbf{P}_l = \left[\mathbf{C}^{-1} + \dfrac{\lambda_l}{Z_l}\mathbf{A}\right]^{-1}$
  3. $\mathbf{S}_l = \mathbf{P}_l\mathbf{E}^{tr}, \quad g_l = \sqrt{\mathbf{S}_l \cdot \mathbf{A}\mathbf{S}_l}, \quad \mathbf{N}_l = \dfrac{1}{g_l}\mathbf{A}\mathbf{S}_l$
  4. $F_l = g_l - Z_l \quad , \quad F_l' = -\left[\dfrac{g_l}{Z_l}\left(1 - \lambda_l\dfrac{Z_l'}{Z_l}\right)\mathbf{N}_l \cdot \mathbf{P}_l\mathbf{N}_l + Z_l'\right]$
  5. $\Delta\lambda = -\dfrac{F_l}{F_l'}$
  6. $|\Delta\lambda| \leq TOL \Rightarrow$ go to 8.
  7. $\lambda_{l+1} = \lambda_l + \Delta\lambda$, $\alpha_{l+1} = \alpha_n + \lambda_{l+1}$, $l \leftarrow l + 1$, go to 1.
  8. Elastic-plastic tangent matrix

     $\mathbf{D}_l = \mathbf{P}_l - \dfrac{\mathbf{P}_l\mathbf{N}_l \otimes \mathbf{P}_l\mathbf{N}_l}{\mathbf{N}_l \cdot \mathbf{P}_l\mathbf{N}_l + H_l} \qquad H_l = \dfrac{Z_l'}{1 - \lambda_l\frac{Z_l'}{Z_l}}$

Viscoplastic stresses and tangent matrix,
Determination of η see Table 2

- $\delta = \dfrac{\Delta t}{\eta} \qquad \beta = \exp(-\delta) \qquad \bar{\mathbf{D}} = \mathbf{D}_l \qquad \bar{\mathbf{S}} = \mathbf{S}_l \qquad \bar{\alpha} = \alpha_l$
- $\mathbf{S}_{n+1} = \beta\ \mathbf{S}_n + (1 - \beta)\,\bar{\mathbf{S}} + \dfrac{1 - \beta}{\delta}\ \mathbf{C}\Delta\mathbf{E}$
- $\alpha_{n+1} = \beta\ \alpha_n + (1 - \beta)\,\bar{\alpha}$
- $\mathbf{E}_{n+1}^{vp} = \mathbf{E}_{n+1} - \mathbf{C}^{-1}\mathbf{S}_{n+1}$
- $\mathbf{D} = (\dfrac{1 - \beta}{\delta})\mathbf{C} + (1 - \beta)\,\bar{\mathbf{D}}$

Table 1: Flowchart for the inelastic stress analysis

2.4 Automatic control of the viscosity parameter

The viscoplastic model is employed to prevent numerical instabilities. The choice of the viscosity parameter η influences the results in a significant way. First of all η must be big enough to guarantee positive diagonal entries of the viscoplastic tangent matrix (14). In contrast to that, η must be small enough, such that the critical energy release rate describes the softening behaviour. Thus, within the present model η is a purely numerical parameter, which requires automatic control for each integration point.

For this purpose, we consider the minimum diagonal term of the rate–independent tangent matrix, thus $R^{pl} = \min(\bar{\mathbf{D}}_{ii})$. Hence, R^{el} is the corresponding quantity within the elastic tangent matrix and R^{Tol} is the tolerance value. Considering (14) we define

$$\frac{1-\beta}{\delta}\, R^{el} + (1-\beta)\; R^{pl} \quad - R^{Tol} \;=\; 0\;, \tag{15}$$

which provides a nonlinear equation in η. An iterative Newton procedure to determine the parameter η is summarized in Table 2. This calculation is performed for every integration point. In the global equilibrium iteration η is constant for the respective time step.

As a test for the automatic control we consider the problem according to Fig. 4. The block with edge length $1\,cm$ is discretized using three eight–node hexahedral elements. Softening occurs within the interface layer of thickness h_t. The material constants are given in Fig. 4, where the softening parameter μ follows from (4).

The displacement u_z is controlled within a geometrically linear calculation. The results of the parameter variation are depicted in Fig. 5. The applied load F is shown versus displacement u_z. For this simple example the rate–independent solution can be calculated numerically. As the plots show, the viscoplastic solution with $\eta \neq 0$ yields higher stresses than the rate–independent solution, so–called over–stresses. Fig. 5a) depicts the postcritical behaviour using different viscosity parameters. The curves approach the rate–independent solution with decreasing η. Only for a very small value of $\eta = 10^{-4}$ complete softening with vanishing normal stress takes place. In this case also a very small time increment is necessary to obtain the regularization effect, see eq. (14). In Fig. 5b) the time increment is modified. Finally, Fig. 5c) shows that only with automatic control of η the interlaminar normal stresses completely vanish independently of the time increment.

- Setup of starting values

$$
\begin{array}{lcl}
R^{pl} & = & D_{ii} = \min\,(D_{jj}) \\
R^{el} & = & C_{ii} \\
R^{Tol} & = & R^{el} * 10^{-6} \\
\eta & = & TOL1 \\
R^{pl} & > & 0 \;\Rightarrow \text{END}
\end{array}
$$

- Iteration

1. $\delta = \dfrac{\Delta t}{\eta}$, $\beta = \exp(-\delta)$, $\omega = 1 - \beta$
2. $\Delta\eta = \dfrac{R^{Tol} - \omega\,\eta\,R^{el} \,/\, \Delta t - \omega\,R^{pl}}{R^{el}\,(\omega \,/\, \Delta t - \beta \,/\, \eta) - \Delta t\,\beta\,R^{pl} \,/\, \eta^2}$
3. $\mid \Delta\eta \mid \leq TOL2 \qquad \Rightarrow$ END
4. $\eta \leftarrow \eta + \Delta\eta \qquad \Rightarrow$ go to 1.

Table 2: Automatic control of the viscosity parameter

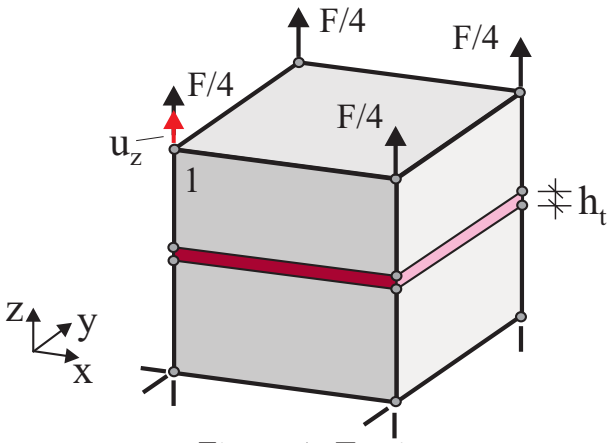

$$
\begin{array}{rcrl}
E_1 & = & 138000 & N/mm^2 \\
E_2 & = & 8960 & N/mm^2 \\
G_{12} & = & 7100 & N/mm^2 \\
G_{23} & = & 3446 & N/mm^2 \\
\nu_{12} & = & 0.3 & \\
Z_0 & = & 51.7 & N/mm^2 \\
R_0 & = & 91.7 & N/mm^2 \\
G_c & = & 0.2585 & N/mm \\
\mu & = & 1.0 & \\
h_t & = & 0.01 & mm
\end{array}
$$

Figure 4: Tension test: geometry and material data

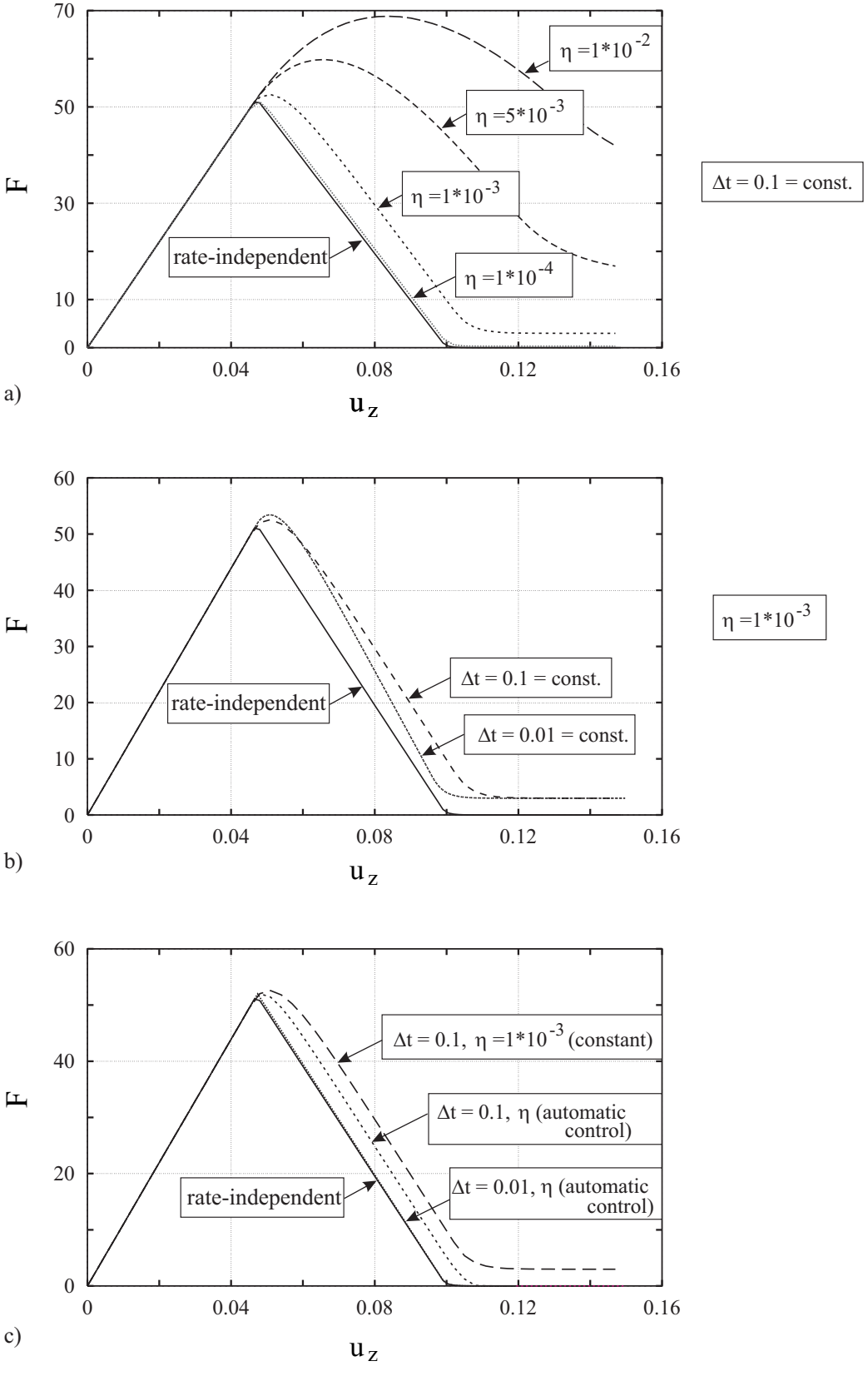

Figure 5: Load displacement curves of point 1

3 Examples

In this section we consider four examples, where primarily the influences of the introduced geometrical and material quantities are investigated. Variations of the energy release rate, the thickness and the fibre angle of the interface layer, the size of the time increment and the mesh density are performed. Comparisons with available experimental results are given.

3.1 Double cantilever beam test

As a the first example we investigate a double cantilever beam with a given initial delamination, see Fig. 6. This type of test specimen is often used to measure the critical mode-I energy release rates. The initial delamination length is adjusted with $a_0 = 31.75\,mm$ accounting for the load device at the cantilever tip. The resultant load $q \cdot b$ amounts to 1.0 kN. We compare our numerical results with experimental investigations of *Aliyu and Daniel* [16]. The authors determined a critical energy release rate $G_c = 0.222\ N/mm$ using a crack opening velocity of $\dot{w} = 0.85\ mm/s$. The material properties for an AS-4/3501-6 graphite epoxy are summarized in Fig. 6. The fiber direction within the whole structure corresponds to the global x–direction .

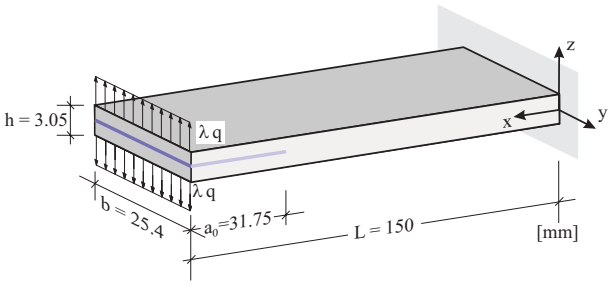

E_1	=	138000	N/mm^2
E_2	=	8960	N/mm^2
G_{12}	=	7100	N/mm^2
G_{23}	=	3446	N/mm^2
ν_{12}	=	0.3	
Z_0	=	51.7	N/mm^2
R_0	=	91.7	N/mm^2
G_c	=	0.222	N/mm

Figure 6: Double cantilever beam: geometry and material data

Due to the symmetry of the structure and loading conditions, only a quarter of the beam has to be discretized. We use two elements in y–direction and three elements in z–direction respectively. The number of elements $n_1 - n_4$ used in the x–direction can be seen in Fig. 7. The thickness of the interface layer is chosen as $h_t = h/100$. The energy release rate is the energy of a body with a certain volume referring to the newly opened delamination area. Since in the present case only the lower part of the beam is discretized, the rate of the energy refers to the corresponding volume fraction, and thus it must be halved. In contrast to

that the symmetry condition in y–direction does not influence μ. In this case the ratio of the energy and the newly opened delamination area remains constant. Thus, the parameter μ is determined via (4) as $\mu = 7.1$.

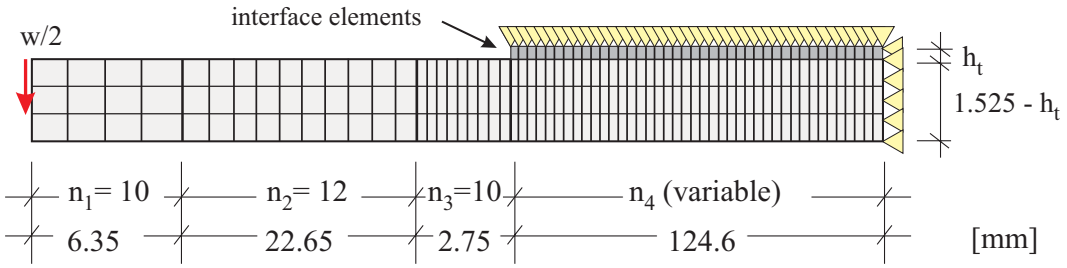

Figure 7: Finite element mesh

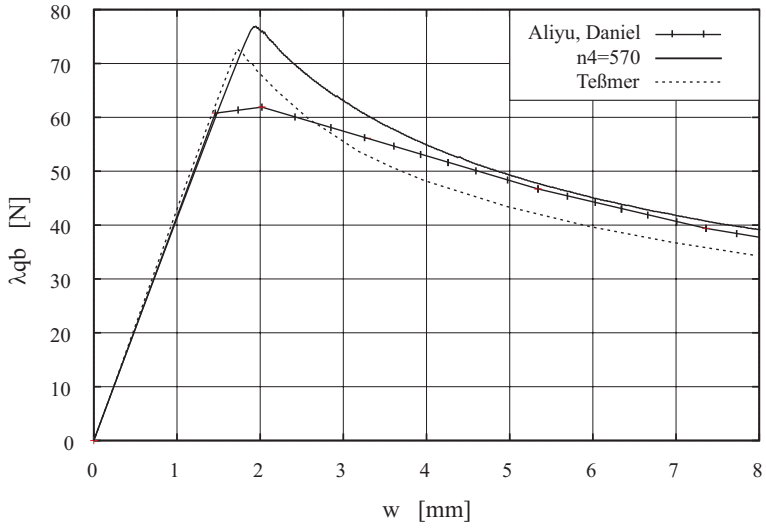

Figure 8: Load deflection curve, experimental and finite element results

The present analysis is performed controlling the tip displacement. In Fig. 8 the load $\lambda\, qb$ is depicted versus the crack opening displacement w, where w denotes the total mutual tip displacement of the beam. Comparisons with the experimental results of *Aliyu and Daniel* [16] and numerical results of *Teßmer* [5] are given. In [5] a virtual crack closure method is implemented in a so–called multi–director shell element, where only one element is used in y–direction. Within the elastic range both numerical solutions agree with the experiment. The crack opening process starts when the transverse tensile strength Z_0 is exceeded. In the softening range we notice very good agreement of our results with the experiments, especially for large displacements w.

The influence of mesh refinement can be seen in Fig. 9. Three different meshes with $n_4 = 268, 570, 860$ elements in the delamination zone are considered. With $n_4 = 570$ elements a sufficiently converged solution is achieved.

Next, the influence of time increment Δt is investigated. Fig. 10 points out that convergence with a reduction of Δt is obtained. Note, that the considerable number of 8000 time steps is necessary to compute the final configuration with the smallest step size $\Delta t = 0.0005$.

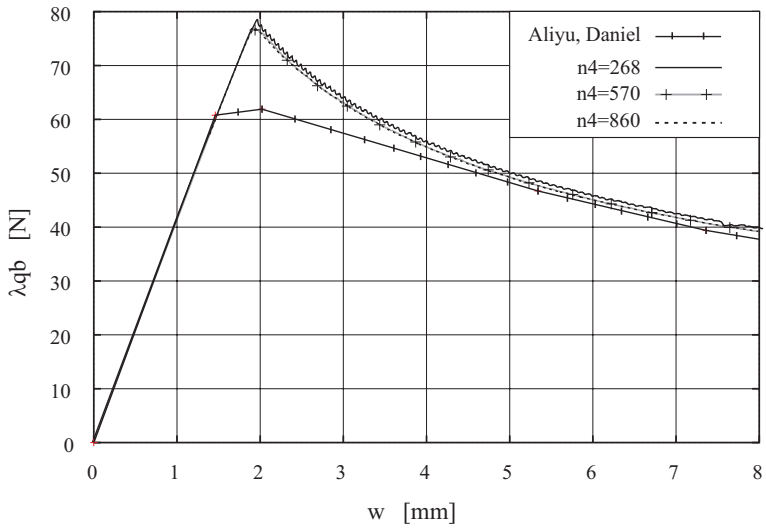

Figure 9: Double cantilever beam, mesh refinement

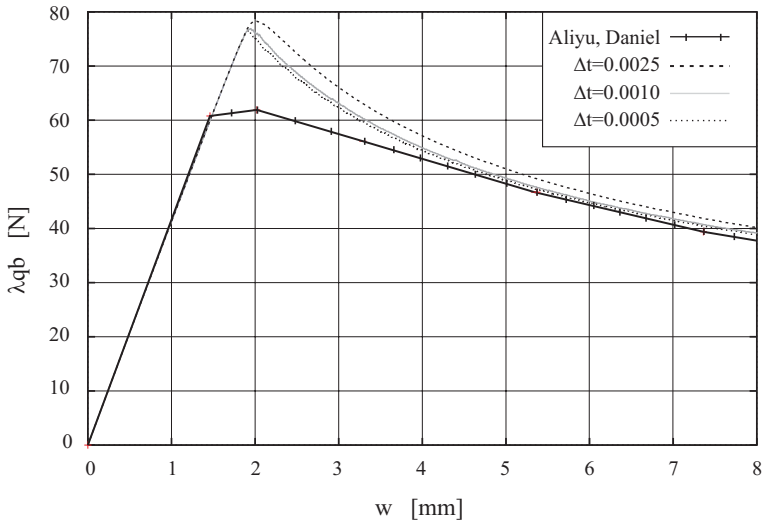

Figure 10: Influence of time step Δt

In Fig. 11 the normal stresses S^{33} are plotted in the x-z-plane for different crack opening displacements. The plots show the concentration of the stresses in front of the crack tip. The stress concentration moves with the propagating delamination front. The newly opened delamination surface is completely free of stresses. Fig. 12 shows the curved boundaries of the delamination zone for different crack opening displacements. This phenomenon is well–known from experiments.

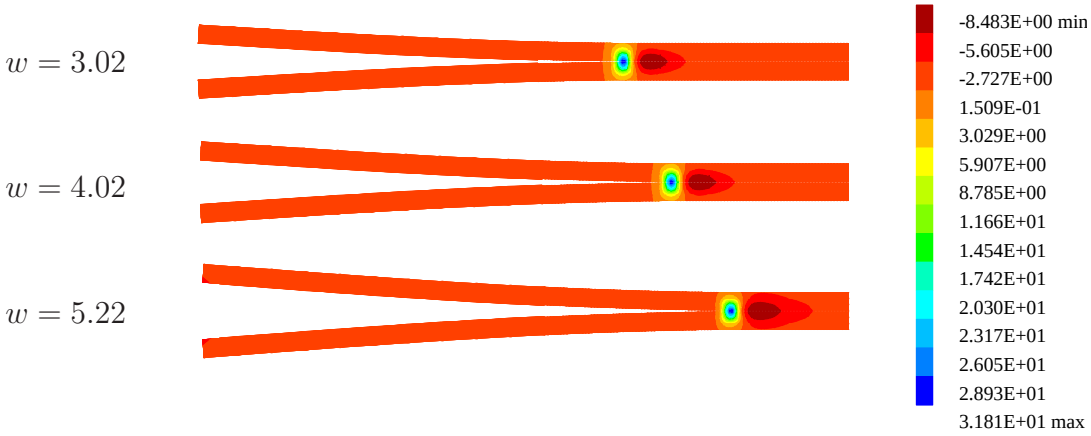

Figure 11: Normal stresses S^{33} in x-z-plane for different crack opening displacements

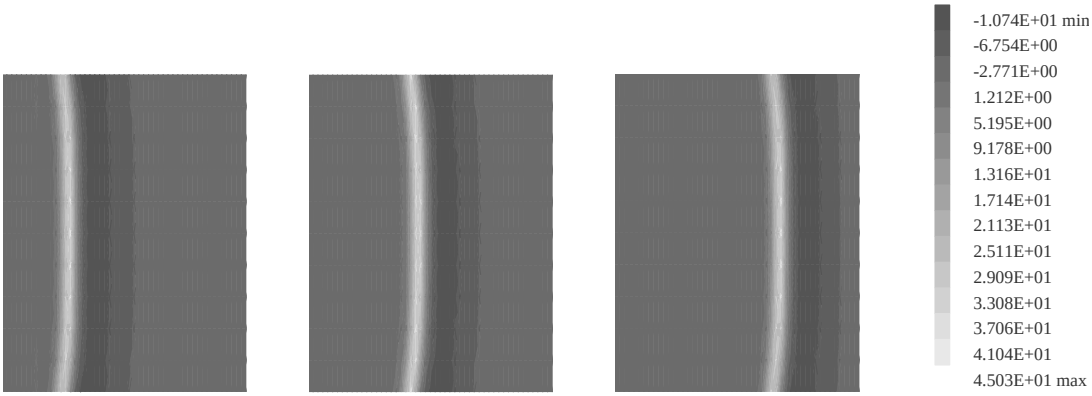

Figure 12: Transverse normal stresses S^{33} in a top view at $w = 2.8, 3.7$ and $4.1\,mm$

3.2 Plate strip with delaminated sublayer

In *Gruttmann and Wagner* [17] and *Sprenger et al.* [13] the stability behaviour of a plate strip with a fixed delamination zone has been investigated. Now we consider the same example, however with propagating delamination. The geometry and material properties are given in Fig. 13.

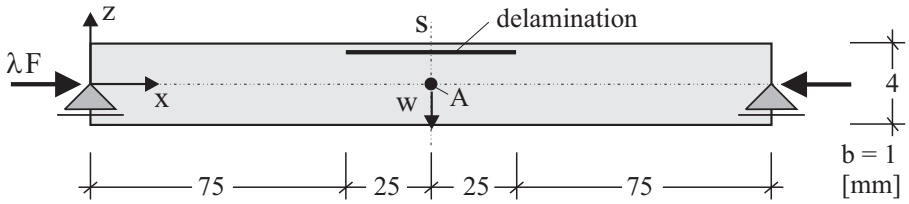

$E_1 = 137900\ N/mm^2$ $\quad G_{12} = 5860\ N/mm^2$

$E_2 = 14480\ N/mm^2$ $\quad G_{23} = 5860\ N/mm^2$

$\nu_{12} = 0.25$ $\quad F = 50\ N$

Figure 13: Delaminated plate strip: geometry and material data

The plate consists of 10 layers with a symmetric stacking sequence $[0°/90°/0°/90°/0°]_s$. Here, 0° refers to the x-direction. The delamination zone lies between layer 9 and 10 in the range $75 \leq x \leq 125$ mm. In Fig. 14 the finite element mesh of half the system with different mesh densities is shown. Furthermore we introduce with n_1, n_2, n_3 the number of elements in length direction in the depicted ranges. The interface layer with thickness h_t is positioned between layer 9 and 10 in the interval of L_2. The discretization in y–direction and z–direction is performed with one and four elements, respectively. The loading is applied via rigid elements. In Fig. 15 two deformed configurations with buckled sublaminate are plotted for a finite element mesh with $n_1 = 12$, $n_2 = 24$ and $n_3 = 24$. In both cases the length of the delamination length L_{del} is given and remains constant. The computed load deflection curves represent lower and upper bounds for the subsequent delamination analysis, see Fig. 16 - 17. In the first case $L_{del} = L_1 = 25\,mm$ and in the second case $L_{del} = L_1 + L_2 = 50\,mm$ are given for half the system, respectively. The external load is increased until the delaminated layer buckles. The non uniform discretization in z–direction represents an imperfection for the system. Thus, with increasing load the plate switches into the secondary solution path without further perturbation. Of course the structure with the short delamination zone $L_{del} = 25\,mm$ yields the higher carrying load. All calculations are done controlling the axial displacement at the support. In the following we perform a variation of the parameters μ and h_t. We choose $n_1 = n_2 = n_3 = 50$ and numerical strength parameters $Z_0 = 0.42\,N/mm^2$, $R_0 = 6.0\,N/mm^2$. Fig. 16 shows a plot of the load factor λ versus the transverse

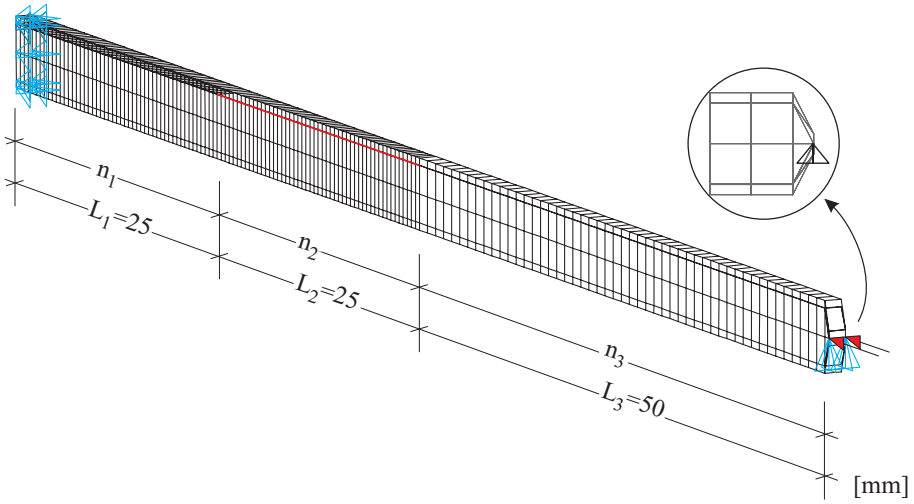

Figure 14: Finite element mesh of the delaminated plate strip

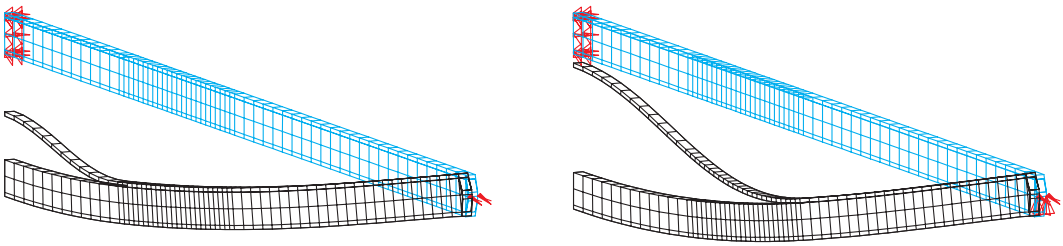

Figure 15: Deformed meshes with short and long delamination zone

displacement w of point A. The curves for the propagating delaminations using four different softening parameters are enveloped by the solutions with fixed delamination lengths. The softening parameter μ is inversely proportional to the critical energy release rate G_c. Thus with increasing μ the delamination zone propagates faster. This behaviour can be observed in Fig. 16. Using a parameter $\mu \geq 0.75$, the delamination develops all over the total range L_2 and the load displacement curve approaches the limit curve. As Fig. 17 for this example shows the influence of h_t on the global deformation behaviour is practically negligible. Furthermore, it has been shown that a numerical integration of the residual vectors and stiffness matrices using four integration points is sufficient for the relative thin interface layers.

Finally, in Fig. 18 the deformed meshes at different load parameters are plotted. To illustrate the delamination progress we define the following parameter

$$D = 100 \frac{Z_0 - Z(\alpha)}{Z_0} \,. \tag{16}$$

Here, $D = 100\,\%$ means that the absolute value of the interlaminar stress vector

is reduced to zero. The plots show that the newly opened surfaces are completely free of stresses.

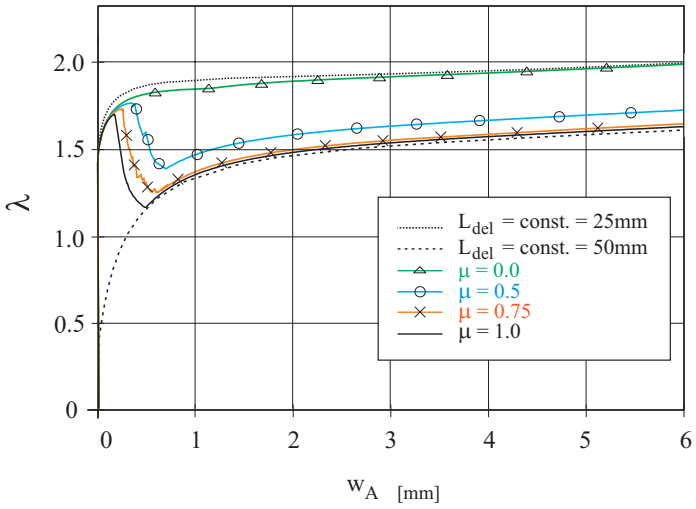

Figure 16: Variation of the softening parameter μ at constant thickness $h_t = 0.02\,mm$

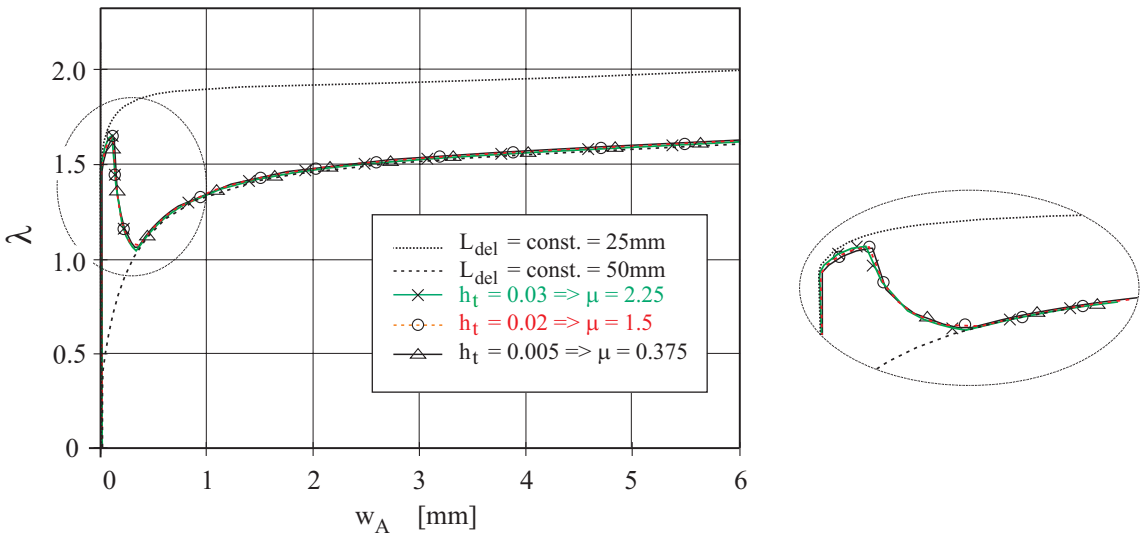

Figure 17: Variation of the thickness h_t at constant energy release rate G_c

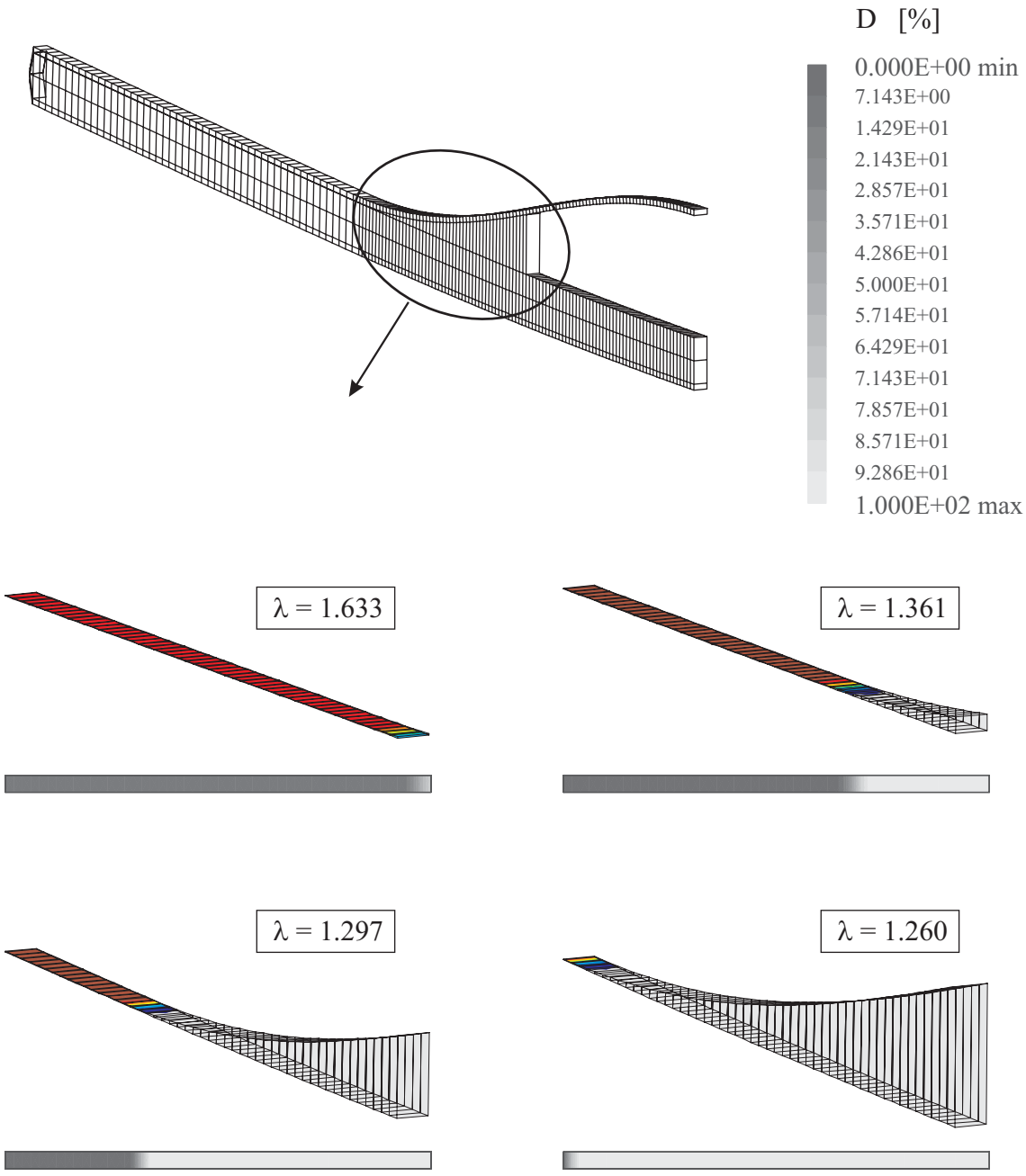

Figure 18: Delamination growth for different load factors λ and constant $\mu = 1.5$

3.3 Plate with initial circular delamination

The next example is a plate consisting of 16 layers with layer thickness $h_L = 0.12\,mm$, and stacking sequence $[0°/0°/+45°/0°/0°/-45°/0°/90°]_S$. A circular delamination is given between layer 14 and 15, see Fig. 19. *Cochelin et al.* [18] investigated the stability behaviour of this structure with nongrowing delaminations. The plate is simply supported along the edges. The geometrical data and the material data for an AS/3501 graphite epoxy composite are given as follows:

$$\begin{array}{lcrlcrl} E_1 & = & 135000 & N/mm^2 & G_{12} & = & 5150 & N/mm^2 \\ E_2 & = & 8500 & N/mm^2 & G_{23} & = & 5150 & N/mm^2 \\ \nu_{12} & = & 0.317 & & & & & \\ Z_0 & = & 51.7 & N/mm^2 & R_0 & = & 91.0 & N/mm^2 \\ h_t & = & 0.005 & mm & F & = & 30 & N/mm \end{array} \tag{17}$$

Due to the fibre angles with $\pm 45°$ the structure is not symmetric with respect to the x-axis and y–axis, respectively. To reduce the computing effort this fact is ignored in the present analysis. The problem of propagating delaminations can in principle be studied when discretizing only one quarter of the plate, see Fig. 19 and Fig. 20. The interface elements are positioned between the layers 14 and 15 only in the fine discretized annular space. In thickness direction several physical layers are summarized within one element layer. This has to be considered when performing the numerical integration in thickness direction, see KLINKEL ET.AL [8] The loads are applied via rigid elements, see Fig. 20. The nonlinear calculations are performed controlling the load parameter λ.

First, we analyze a "perfect" plate without delamination and thus without the interface layer. Due to the symmetric layup the plate is loaded as a pure membrane. With increasing axial deformation a bifurcation point is found at load factor $\lambda = 50.3$. A switch to the secondary solution path is possible by a perturbation with the first eigenvector. Next, we analyze the behaviour of the plate with artificial and non growing delamination. One obtains a stress problem due to the delaminated layer which has the effect of an imperfection. In this case one obtains a load displacement curve which for large displacements approaches the secondary solution path of the perfect plate, see Fig. 21.

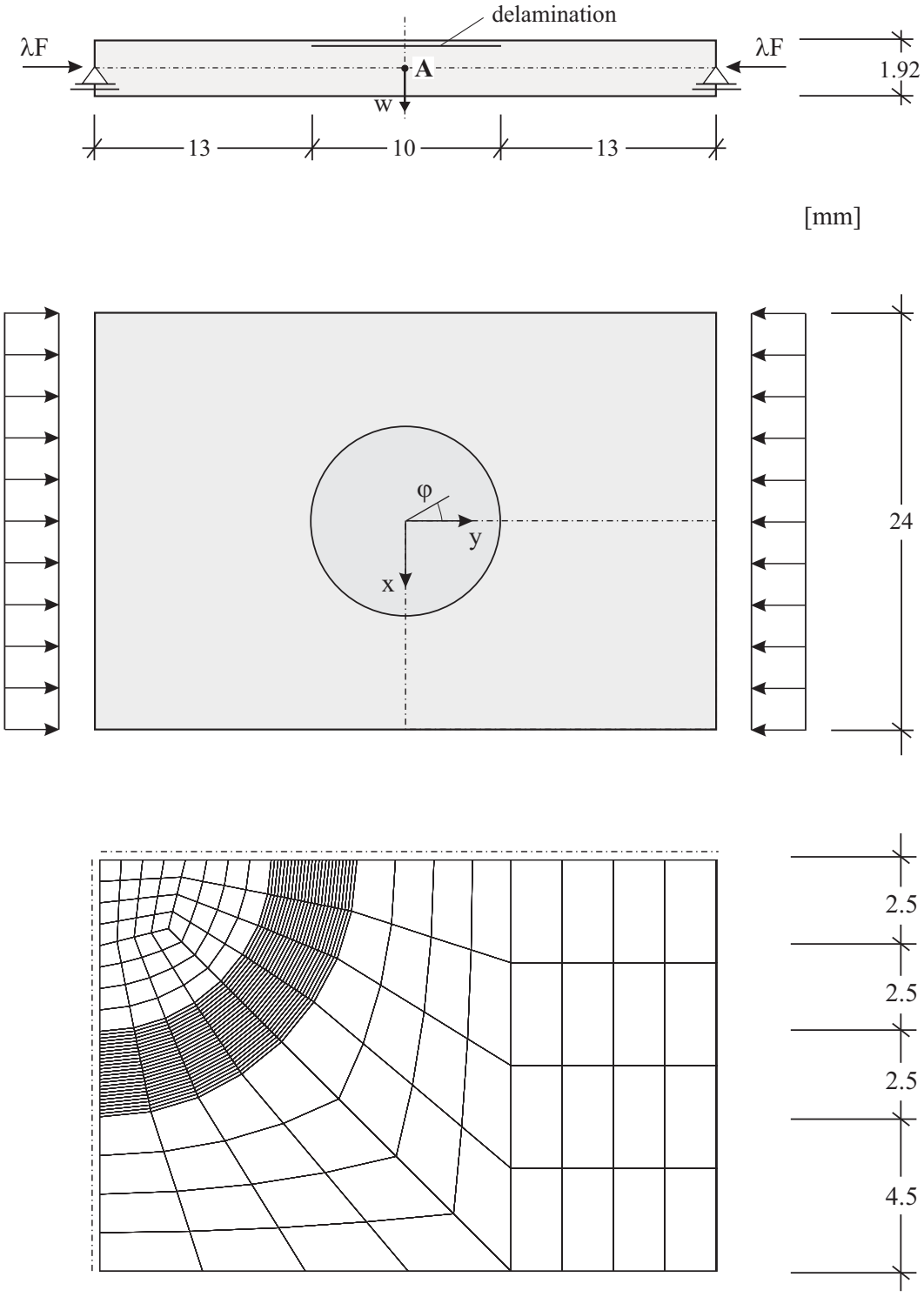

Figure 19: Plate with circular delamination: geometry and finite element mesh

In the following, the influence of the softening parameter μ, the size of the time step Δt and the fibre angle φ within the interface layer, are investigated. The load deflection curves in Fig. 21 shows the variation of the softening parameter μ, and thus the influence of G_c for propagating delaminations. Considering eq. (4) a parameter $\mu = 0.58$ corresponds to an energy release rate $G_c = 0.222 N/mm$, which is a realistic value. The largest value of $\mu = 0.88$ corresponds to $G_c = 0.147 N/mm$. Noticeable differences occur in the range of moderate displacements. This is due to the fact that for finite deformations global buckling dominates the behaviour. Next, two different time steps Δt are chosen. There are only minor differences according to Fig. 22. Furthermore, Fig. 23 shows that the influence of the fiber angle within the interface layer is neglectable.

Delamination starts at the coordinates $(x = 0\,mm, y = 5\,mm)$ and propagates along the inner circle. With increasing load a second point with coordinates $(x = 5\,mm, y = 0\,mm)$ becomes critical. Hence, both delamination ranges fuse. The whole process is depicted in Fig. 24.

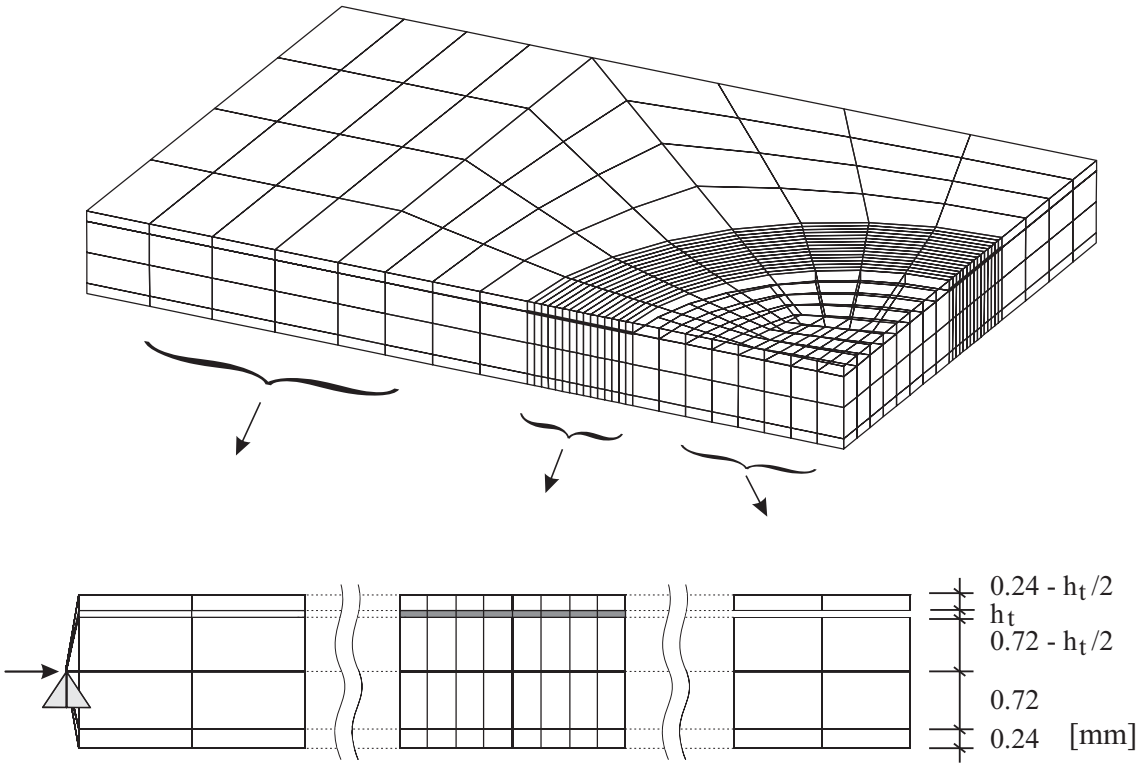

Figure 20: Finite element discretization of one quarter of the plate

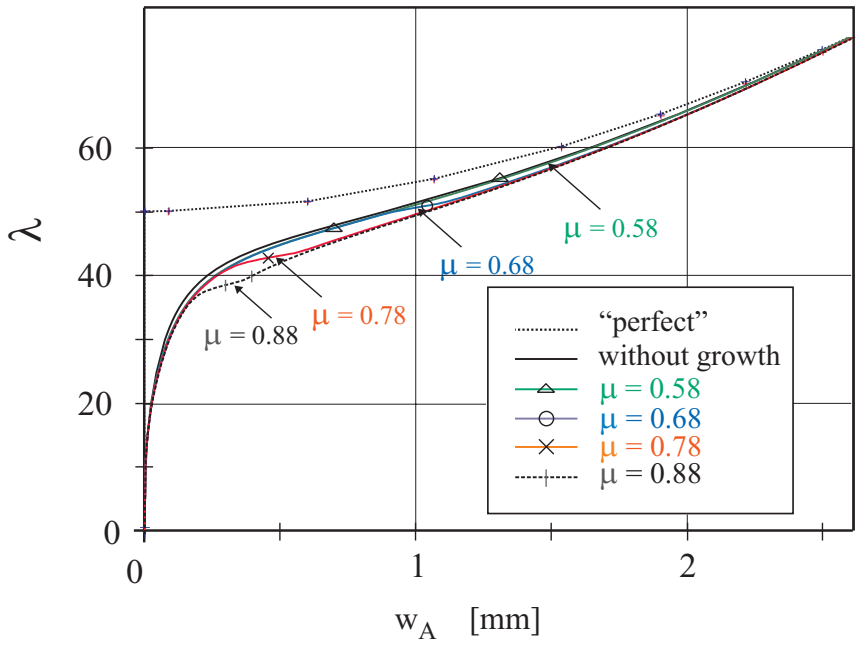

Figure 21: Variation of the softening parameter μ with constant $\Delta t = 0.1$ and $\varphi = 0°$

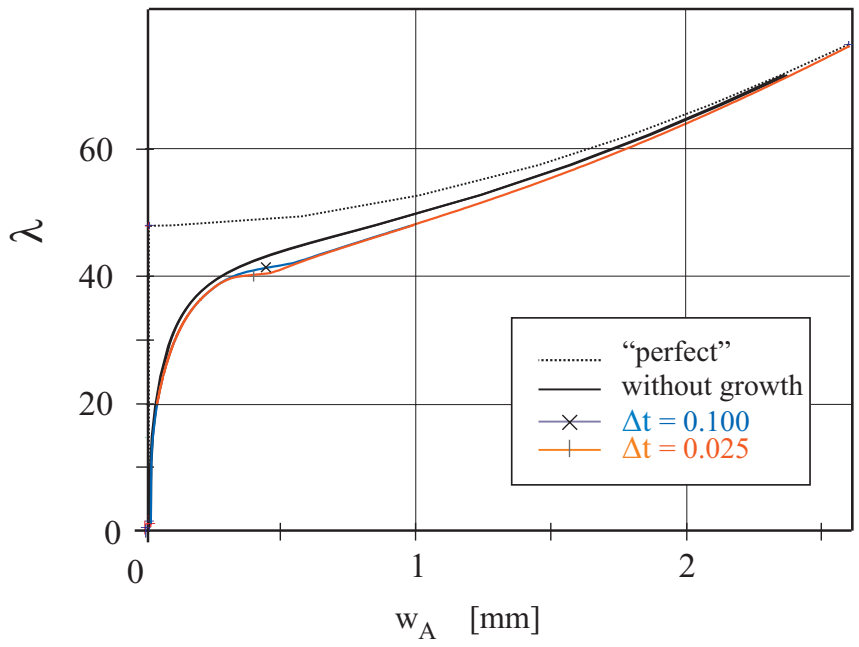

Figure 22: Variation of the time step Δt with constant $\mu = 0.78$ and $\varphi = 0°$

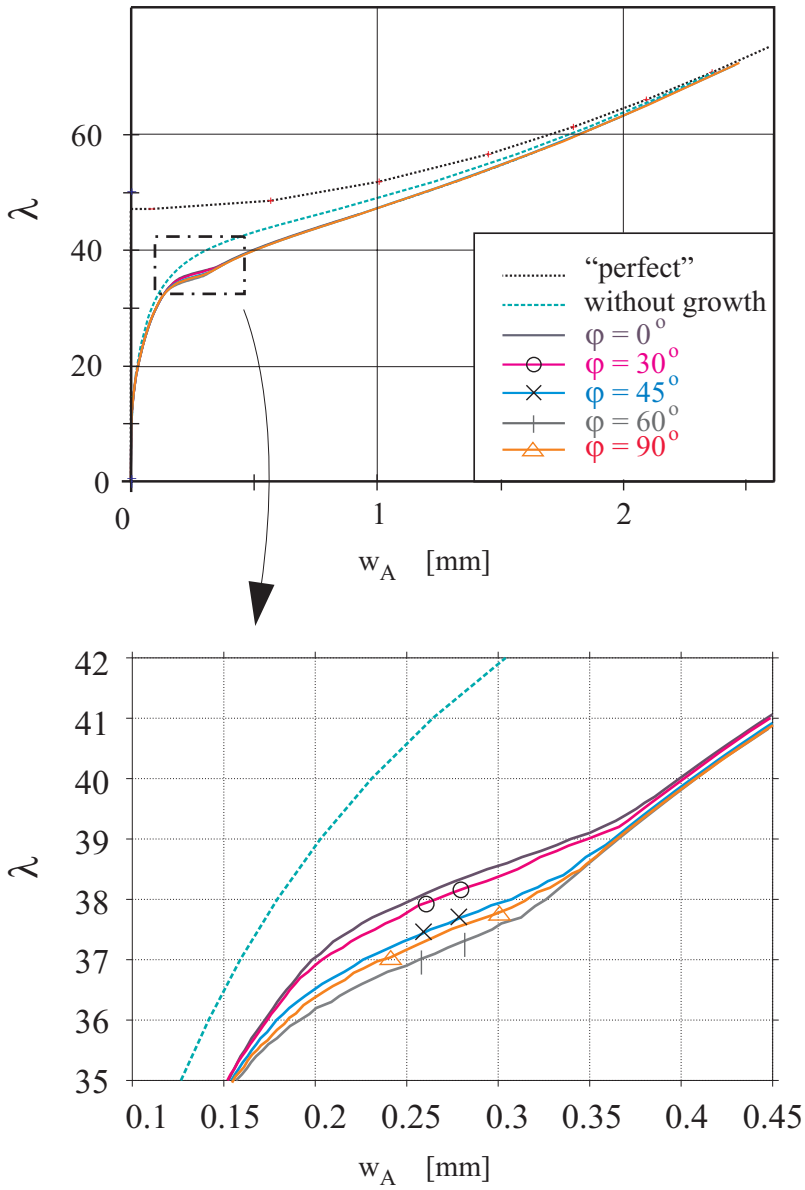

Figure 23: Variation of the fiber angle φ within the interface layer with constant $\Delta t = 0.1$ and $\mu = 0.88$

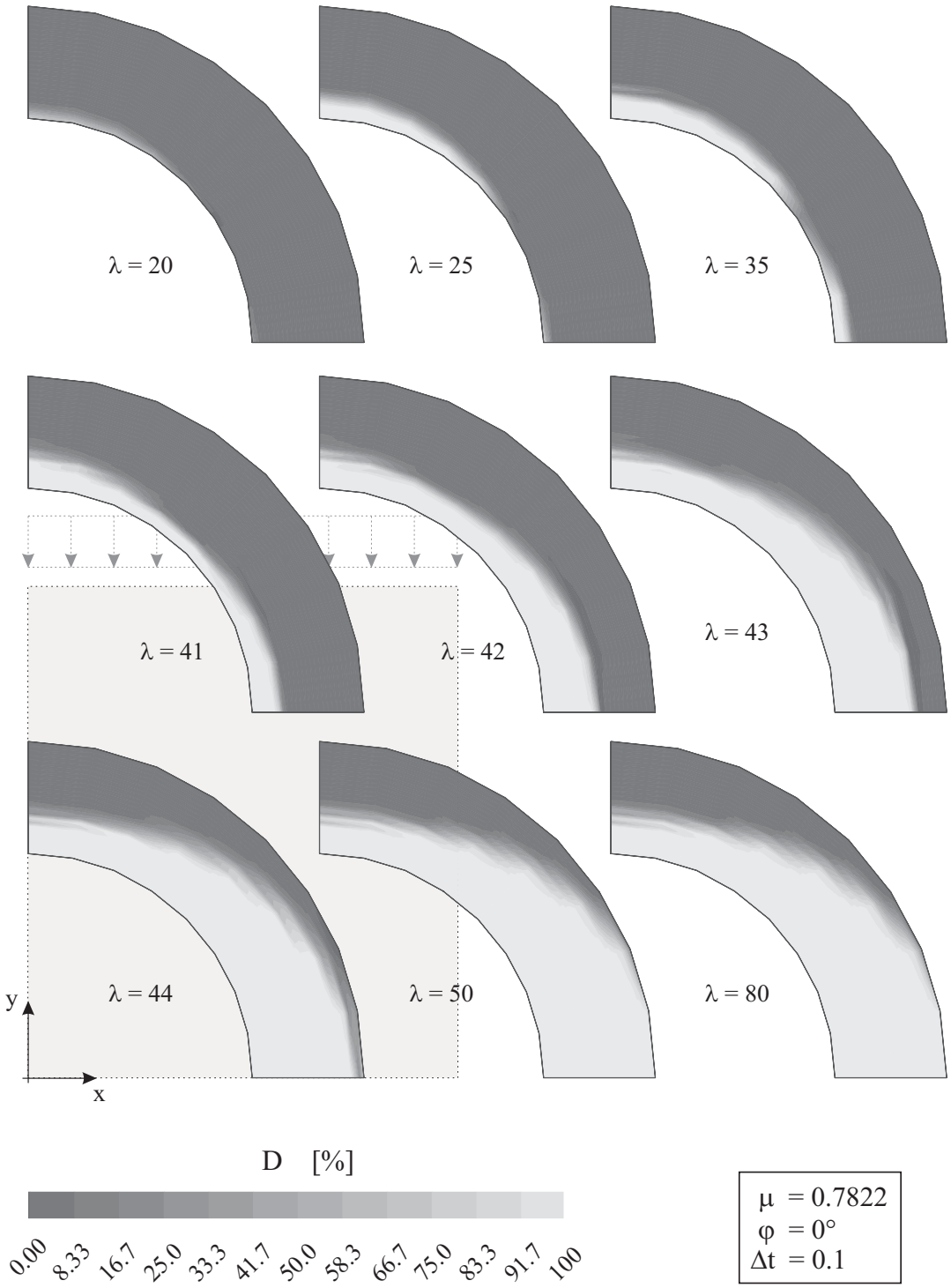

Figure 24: Growing delamination zone

3.4 Carbon fiber reinforced plate

With the last example we consider a plate with a circular hole, see Fig. 25. This type of specimen has been investigated numerically in [19]. Energy release rates have been calculated along measured delamination curves. The experiments with dynamic cyclic loading have been carried out by the DLR (Deutsches Zentrum für Luft- und Raumfahrt, Institut für Strukturmechanik, Braunschweig). The symmetric stacking sequence of the layered plate with 18 layers is given as $[0°/90°/0°//(30°/-30°)_3]_S$, where the fiber angle $\varphi = 0°$ corresponds to the x–axis. The layer thickness is $h_L = 0.125\,mm$. The geometrical data and the material data for a carbon fiber reinforced polymer T300/914C are given in (18). The dynamic effects of the experiments with several thousands of load cycles are considered here with reduced values Z_0 and R_0. Thus, the strength ratios do not represent measured realistic quantities. Here, we determine the growing delamination zone using the developed model for static loading and compare with the experimental results.

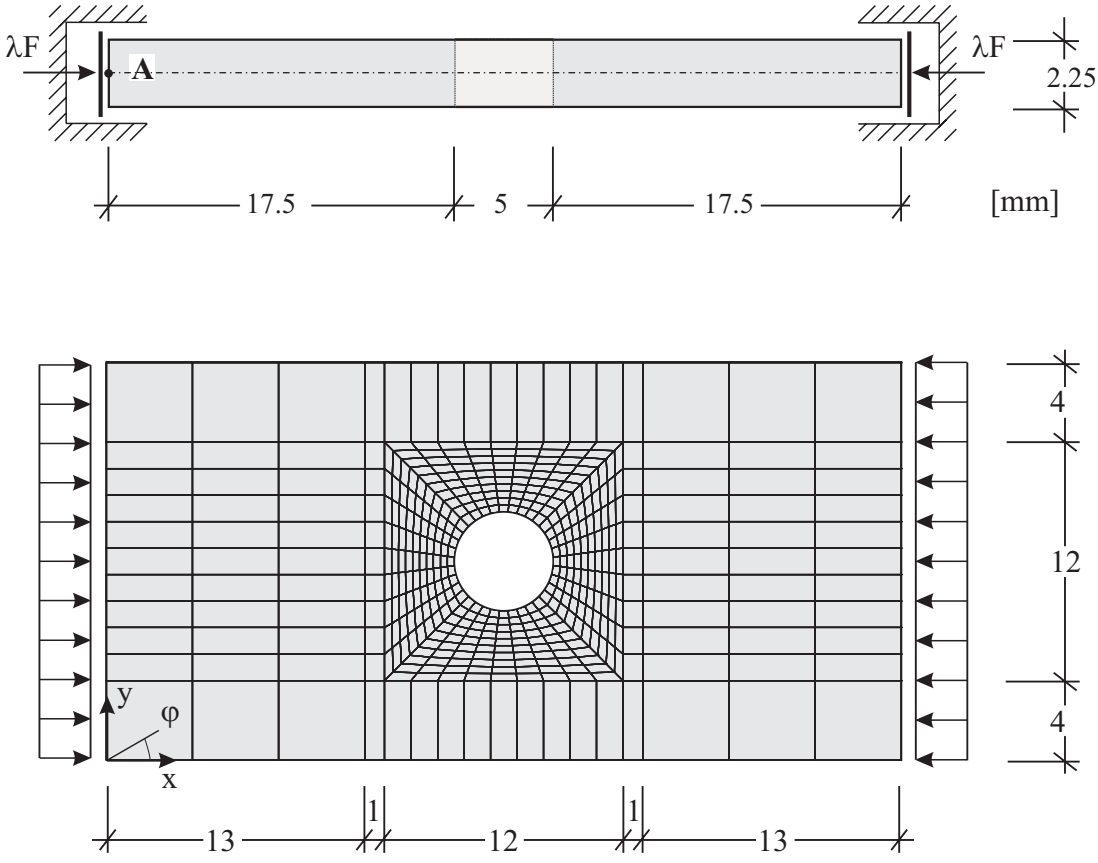

Figure 25: Geometrical data of a fiber reinforced plate

$$
\begin{array}{rclrrclr}
E_1 & = & 129000 & N/mm^2 & G_{12} & = & 3200 & N/mm^2 \\
E_2 & = & 9400 & N/mm^2 & G_{23} & = & 4300 & N/mm^2 \\
\nu_{12} & = & 0.32 & & \mu & = & 0.2 & \\
Z_0 & = & 0.05 & N/mm^2 & R_0 & = & 0.06 & N/mm^2 \\
h_t & = & 0.00125 & mm & F & = & 10 & N/mm
\end{array}
\tag{18}
$$

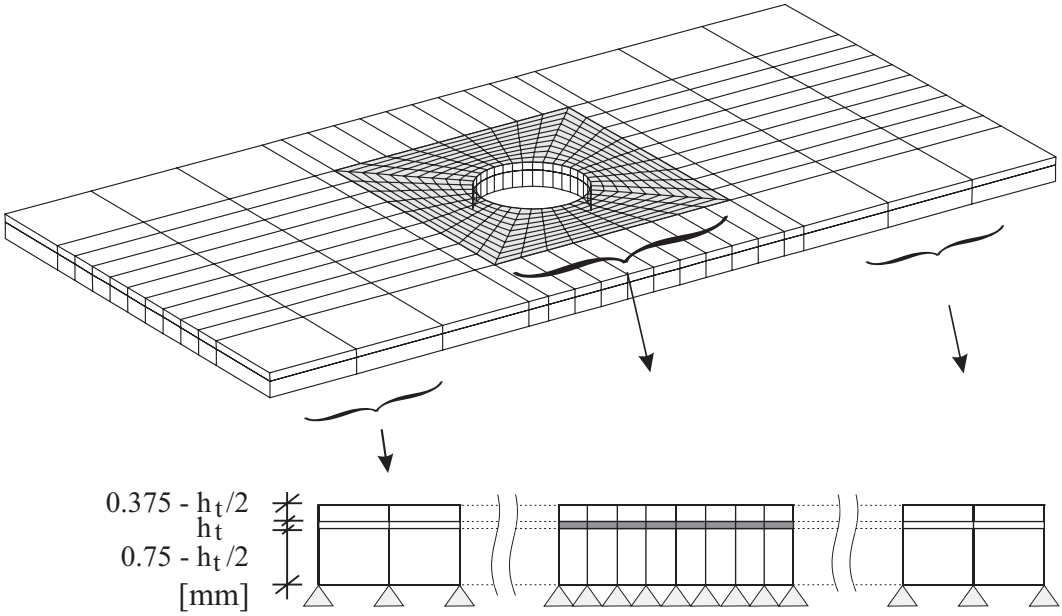

Figure 26: Laminated plate with circular hole

Constant pressure loads are applied along the shorter edges, whereas the other boundaries are free. Fig. 26 shows the finite element mesh. The stress field and the delaminations between the 0°–layer and the 30°–layer are symmetric with respect to the middle plane of the plate. This has also been shown by the experiments. Therefore, only the upper half of the plate is discretized exploiting symmetry conditions. The arrangement of the interface elements can be seen in Fig. 26. The physical layers are summarized in the upper and the lower finite element layer.

The growing delamination ranges are plotted in Fig. 27. The solid lines depict the measured delamination curves. One can see the qualitative agreement of the experimental results with the numerically computed delamination zone. Future investigations should apply local mesh refinement, especially in thickness direction, to obtain more accurate interlaminar shear and normal stresses.

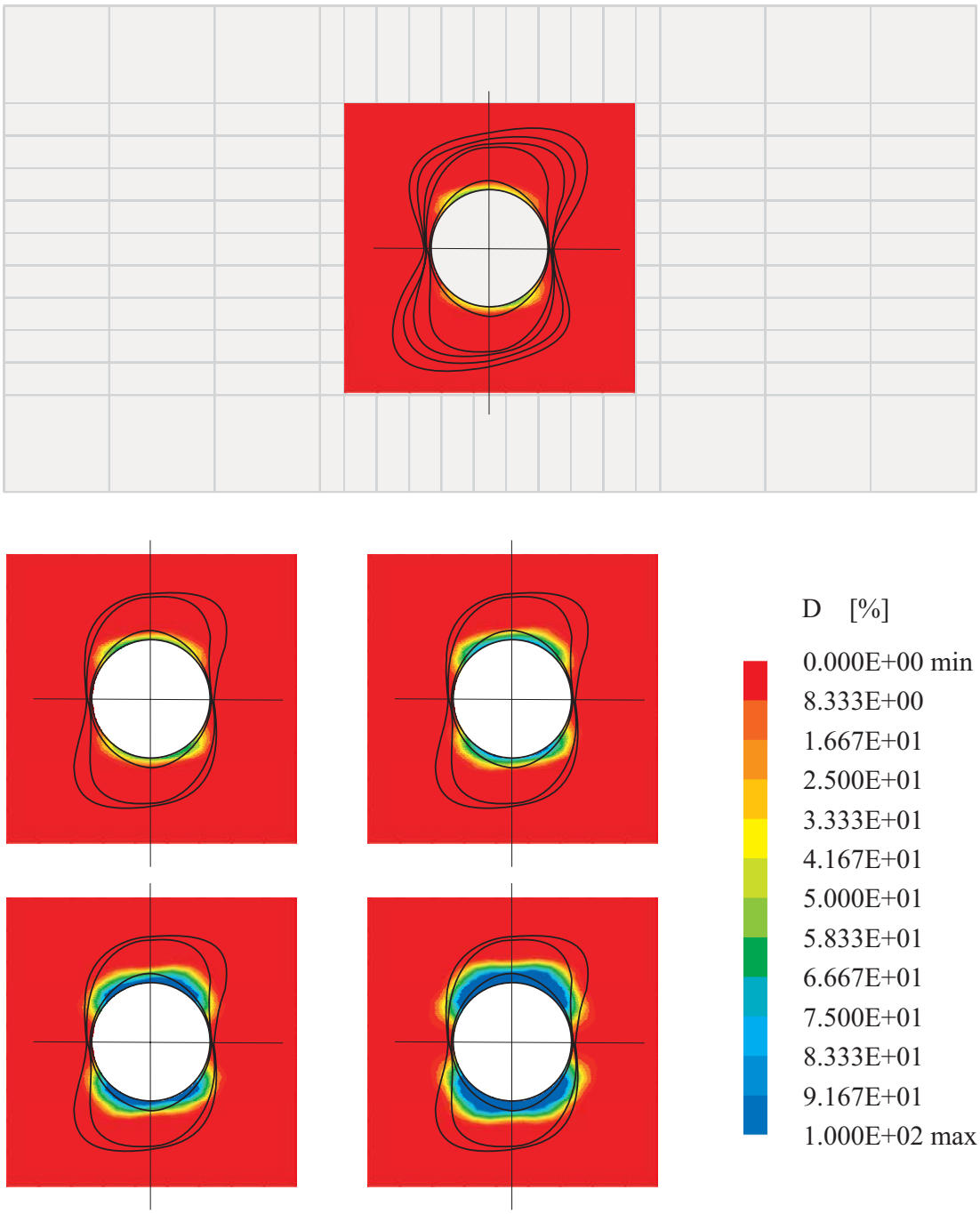

Figure 27: Delamination growth: Experimental and numerical results

Conclusions

This paper presents a finite element method to simulate increasing delaminations in composite structures. Interface layers are discretized using refined eight–node hexahedrons. These elements have a small, but non–vanishing thickness and are located in those regions where delaminations are expected. Within an inelastic model, the delamination criterion of Hashin is extended to a yield criterion with softening. Numerical instabilities are avoided by a viscoplastic regularization. The viscosity parameter is determined automatically such that the critical energy release rate is the essential material parameter. Detailed numerical calculations show the effectivity, robustness and reliability of the developed delamination model. An explicit method may be an alternative effective approach to reduce the computing time. This has been discussed in [9] and is part of future research.

Acknowledgment

The financial support of the Deutsche Forschungsgemeinschaft (DFG) is gratefully acknowledged.

References

[1] Lee JD. Three Dimensional Finite Element Analysis of Damage Accumulation in Composite Laminate. *Computers & Structures* 15(3) (1982), 335–350. 1

[2] Hashin Z. Failure Criteria for Unidirectional Composites. *J. Appl. Mech.* 47 (1980), 329–334. 1, 2.1

[3] Davidson BD. An Analytical Investigation of Delamination Front Curvature in Double Cantilever Beam Specimens. *Journal of Composite Materials* 24 (1990), 1124–1137. 1

[4] Wang ASD, Slomiana M, Bucinell RB. Delamination Crack Growth in Composite Laminates. In: Johnson, W.S. (Eds.), *Delamination and Debonding of Materials*, ASTM, 135–167, Philadelphia, 1995. 1

[5] Teßmer J. Theoretische und algorithmische Beiträge zur Berechnung von Faserverbundschalen. Report F00/3 (in German), Institut für Baumechanik und Numerische Mechanik, Universität Hannover, 2000. 1, 3.1

[6] Schellekens JC, De Borst R. Free Edge Delamination in Carbon-Epoxy Laminates: a Novel Numerical/Experimental Approach. *Composite Structures* 28 (1994), 357–373. 1

[7] Crisfield MA, Jelenic G, Mi Y, Zhong HG, Fan Z. Some Aspects of the Nonlinear Finite Element Method. *Finite Elements in Analysis and Design* 27 (1997), 19–40. 1

[8] Klinkel S, Gruttmann F, Wagner W. A Continuum Based Three-Dimensional Shell Element for Laminated Structures. *Computers & Structures* 71 (1999), 43–62. 1, 2, 3.3

[9] Wagner W, Gruttmann F. Problemorientierte Modellierung von Faserverbund-Strukturen. Research report on contract Deutsche Forschungsgemeinschaft WA746/6-1. 1, 3.4

[10] Bathe KJ, Dvorkin E. A Continuum Mechanics Based Four Node Shell Element for General Nonlinear Analysis. *Engineering Computations* 1 (1984), 77–88. 2

[11] Betsch P, Stein E. An Assumed Strain Approach Avoiding Artificial Thickness Straining for a Nonlinear 4-Node Shell Element. *Communications in Numerical Methods in Engineering* 11 (1995), 899–910. 2

[12] Simo JC, Rifai D. A Class of Mixed Assumed Strain Methods and the Method of Incompatible Modes. *Int. J. Num. Meth. Engng.* 29 (1990), 1595–1638. 2

[13] Sprenger W, Gruttmann F, Wagner W. Delamination growth analysis in laminated structures with continuum based 3D-shell elements and a viscoplastic softening model. *Computer Methods in Applied Mechanics and Engineering* 185 (2000), 123–139. 2.1, 2.1, 2.2, 3.2

[14] Duvaut G, Lions JL. *Les Inequations en Mechanique et en Physique.* Dunod, Paris, 1972. 2.3

[15] Simo JC, Kennedy JG, Govindjee S. Non–Smooth Multisurface Plasticity and Viscoplasticity. Loading/Unloading Conditions and Numerical Algorithms. *Int. J. Num. Meth. Engng.* 26 (1988), 2161–2185. 2.3

[16] Aliyu AA, Daniel IM. Effects of Strain Rate on Delamination Fracture Toughness of Graphite/Epoxy. In: Johnson WS, (editor), *Delamination and Debonding of Materials, ASTM STP 876*, 336–348, Philadelphia, 1985. 3.1, 3.1

[17] Gruttmann F, Wagner W. On the Numerical Analysis of Local Effects in Composite Structures. *Composite Structures* 29 (1994), 1–12. 3.2

[18] Cochelin B, Damil N, Potier-Ferry M. Asymptotic-Numerical Methods and Padé Approximants for Nonlinear-Elastic Structures. *Int. J. Num. Meth. Engng.* 37 (1994), 1137–1213. 3.3

[19] Stein E, Gruttmann F, Meyer R, Ohnimus S, Peters K, Rust W, Wagner W, Zhang G. Numerische Untersuchungen an zwei gelochten CFK-Proben. Research report on contract DLR 5–131–4303, (1991), internal report. 3.4